Nigerian Journal of Applied Physics (NJAP)
ISSN Print: 3115-5871
ISSN Online: 3115-588X
DOI: https://doi.org/10.62292/njap-v2i3-2026-100
Volume 2(3), September 2026

Thermal, Resistive, Optical, And Recombination Loss Mechanisms In Coumarin-343-Based Solid State Dye Sensitized Solar Cells: A Numerical Performance Analysis

***[1]Sani Marwan, [1]Adeyemi Joshua Owolabi, [1]Christiana Onma, [1]Rabiu Abubakar Tafida and [2]Abdulahi Lawal**

[1]Department of Physics, Faculty of Science, Nigerian Defense Academy, Kaduna State, Nigeria.
[2]Department of Physics, Ahmadu Bello University, Zaria, Kaduna State, Nigeria.

*Corresponding author's email: marwansani21@gmail.com

ABSTRACT

Solid-state dye-sensitized solar cells (ssDSSCs) based on organic sensitizers offer a low-cost route to photovoltaic conversion, but their practical performance is limited by thermal, optical, resistive, and recombination losses. This study numerically investigated these loss mechanisms in a Coumarin-343 (C343)-based ssDSSC using SCAPS-1D version 3.3.10. A reference FTO/TiO_2/C343/Spiro-OMeTAD/Au device was first established and then optimized through transport-layer selection, thickness variation, and defect-density analysis. The optimized simulated architecture was FTO/Tm-TiO_2/C343/PEDOT:PSS/Au, with 0.5 μm Tm-TiO_2, 0.7 μm C343, 0.5 μm PEDOT:PSS, and a C343 defect density of 1×10^{15} cm^{-3}. Under standard simulated conditions, the optimized device achieved Voc = 1.294 V, Jsc = 9.430 mA cm^{-2}, FF = 81.90%, and PCE = 9.99%, compared with 3.40% for the reference device. Thermal analysis from 300–360 K showed that PCE increased slightly to 10.08% around 330 K before declining at higher temperature because of voltage loss. Increasing series resistance mainly reduced fill factor, while low shunt resistance caused severe voltage and efficiency degradation. Optical reflection reduced current generation, whereas radiative and Auger recombination lowered Jsc and PCE. Under combined non-ideal conditions, the simulated PCE decreased to 0.068%. These results show that shunt suppression, defect/interface passivation, low series resistance, optical management, and thermal control are critical for translating simulated C343 ssDSSC performance into realistic device designs.

Keywords:
Coumarin-343,
Solid-State Dye-Sensitized Solar Cell,
Thermal Loss,
Series Resistance,
Shunt Resistance.

INTRODUCTION

Dye-sensitized solar cells separate the tasks of light absorption and charge transport of a molecular dye captures incident photons, while a semiconductor and a whole transport medium provide the pathways for electron and hole extraction. This architecture has made DSSCs attractive as a low cost photovoltaic technology, particularly because their fabrication can be simpler than that of crystalline silicon devices and their performance under diffuse illumination can remain useful (Hagfeldt et al., 2010; Kokkonen et al., 2021). The replacement of the liquid electrolyte by a solid hole transport material has further addressed problems associated with solvent evaporation, leakage, corrosion, and sealing. These changes, however, do not remove the electronic and thermal losses that ultimately determine the delivered power of a practical device (Benesperi et al., 2018; Wang et al., 2020).

Coumarin dyes are particularly interesting because they are metal free organic sensitizers whose molecular structure can be modified to tune light absorption and charge transfer characteristics. Coumarin-343 (C343) has been investigated as a representative sensitizer, but its photovoltaic response remains strongly dependent on the dye and semiconductor interface, charge injection, and recombination kinetics (Koops et al., 2010; Liu et al., 2013). The literature survey places experimental C343-based DSSCs mainly in the few percent efficiency range, with reported PCEs of about 3.7–5.6% depending on the transport materials and co-sensitization strategy as shown in Table 1. These values provide a useful context for assessing how much of the simulated performance is gained by device optimization and how much can subsequently be lost when non ideal operating conditions are introduced.

Table 1. Reported Photovoltaic Performance of C343 Based Devices

Device/configuration	Voc (V)	Jsc (mA cm⁻²)	FF	PCE	Reference
TiO_2/C343/I^-/I_3^- DSSC	0.68–0.72	7.8–8.5	0.69–0.73	3.7–4.2%	Wang et al. (2014)
TiO_2/C343 + Co(II/III) electrolyte	0.80–0.84	6.5–7.0	0.70	4.0–4.3%	Karaca et al. (2025)
TiO_2/C343 + D131 co-sensitizer	0.75	10.2	0.73	5.6%	Zhang et al. (2012)
DFT-optimized TiO_2/C343	0.73–0.78	8.0–8.8	0.75	4.8–5.0%	Liu et al. (2013)
C343/ZnO DSSC	0.64	5.3	0.65	2.2%	Kumari Shukla & Sekar (2024)

Because the optimized efficiencies obtained in SCAPS-1D can exceed experimentally reported values when idealized parameters, low defect densities, or weak parasitic losses are assumed, simulated results must be interpreted as performance limits rather than direct experimental predictions. Saidarsan et al. (2025) emphasized that unrealistic SCAPS-1D outputs can arise when simulations are not benchmarked against experimental ranges or tested under non-ideal electrical and optical conditions. In this context, the present study uses the optimized C343-based efficiency as a reference ceiling and then evaluates how temperature, resistance, reflection, and recombination lower the attainable performance.

The central issue addressed here is not simply how to obtain a high simulated efficiency, but how that efficiency responds when the device is exposed to conditions that represent real losses. In a solar cell, series resistance dissipates electrical power that bends the current voltage curve, whereas shunt resistance provides a leakage path that can severely reduce voltage and fill factor. Temperature affects carrier populations, recombination rates, transport, and the quasi Fermi level splitting. Optical reflection reduces the photon flux reaching the sensitizer, while radiative, Auger, and defect assisted recombination remove carriers before they can be collected. These mechanisms act through different physical pathways, so treating them separately provides a clearer indication of which engineering variable should receive priority (Bisquert, 2002; Green, 1982; Maçaira et al., 2015).

MATERIALS AND METHODS

Device structure and simulation framework

The device was modeled with SCAPS-1D version 3.3.10 using a one dimensional drift diffusion description. The simulator solves Poisson's equation together with the electron and whole continuity equations and incorporates optical generation, carrier transport, and recombination within the layered structure (Burgelman et al., 2000). The basic architecture was FTO/ETL/C343/HTL/Au. The reference configuration used TiO_2 and Spiro-OMeTAD, while the optimization stage compared alternative metal doped TiO_2 electron transport layers and solid whole transport materials. All standard simulations were performed at AM1.5G illumination, 100 mW cm⁻², and 300 K.

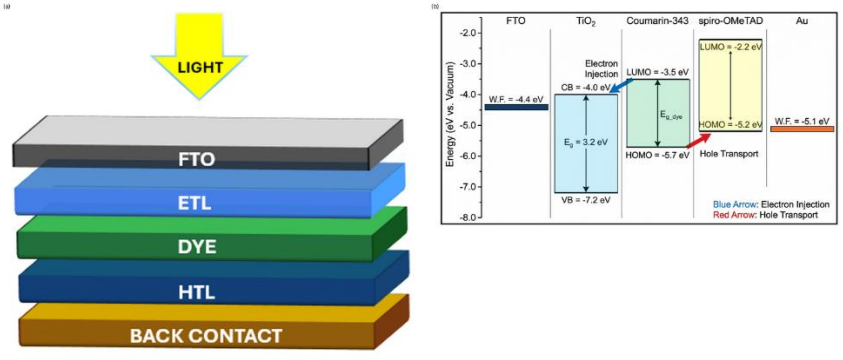


Figure 1. Device architecture and energy level representation used in the numerical study

Table 2 summarizes the principal material parameters used for the baseline FTO/TiO_2/C343/Spiro-OMeTAD stack. The C343 layer was treated as the absorbing active layer, with an initial thickness of 200 nm, bandgap of 2.5 eV, electron affinity of 3.6 eV, and electron mobility of 100 cm² V⁻¹ s⁻¹. The interface model contained neutral defect states at both the ETL/C343 and C343/HTL boundaries, each specified as a two-dimensional interface density of 1×10^{15} cm⁻², with electron and whole capture cross sections of 1×10^{-19} cm². The trap level was positioned at Et = 0.6 eV below the conduction-band edge, Ec, for both interfaces. These interface states are important for the research because the baseline generation

and recombination profiles show that the interfaces are active regions for carrier loss.

Table 2: Principal C343 ssDSSC Simulation Parameters

Parameter	FTO	TiO_2	C343	Spiro-OMeTAD
Thickness (nm)	20	100	200	100
Bandgap, Eg (eV)	3.5	3.2	2.5	2.8
Electron affinity, χ (eV)	4.0	3.9	3.6	2.52
Relative permittivity, εr	9	9	3.5	3
Electron mobility, μe ($cm^2\ V^{-1}\ s^{-1}$)	20	20	100	100
Hole mobility, μh ($cm^2\ V^{-1}\ s^{-1}$)	10	10	25	25
Acceptor density, NA (cm^{-3})	0	0	1.0×10^{16}	1.0×10^{17}
Donor density, ND (cm^{-3})	1.0×10^{21}	1.0×10^{16}	1.0×10^{16}	0
Defect density, Nt (cm^{-3})	1.0×10^{15}	1.0×10^{15}	1.0×10^{15}	1.0×10^{15}

Table 3: Interface State Parameters Used To Represent Surface Recombination

Interface parameter	ETL/C343 interface	C343/HTL interface
Defect type	Neutral	Neutral
Total interface density (cm^{-2})	1.0×10^{15}	1.0×10^{15}
Electron capture cross-section (cm^2)	1.0×10^{-19}	1.0×10^{-19}
Hole capture cross-section (cm^2)	1.0×10^{-19}	1.0×10^{-19}
Trap energy level, Et, relative to Ec (eV)	0.6	0.6

Transport Layer Selection and Parameter Optimization

The subsequent loss analysis is performed on an optimized device while the material and thickness screening results are retained only where they establish the electrical baseline. Four doped TiO_2 variants such as Mg-TiO_2, Nb-TiO_2, Tm-TiO_2, and Sn-TiO_2 were compared with pristine TiO_2. The parameter sets used in this screening are given in Table 4. Tm-TiO_2 had a 2.6 eV bandgap, electron affinity of 3.9 eV, electron mobility of 20 $cm^2\ V^{-1}\ s^{-1}$, and donor density of $1 \times 10^{16}\ cm^{-3}$. The corresponding HTL comparison included CuI, Cu_2O, PEDOT: PSS, and PTAA alongside Spiro-OMeTAD as shown in Table 5.

Table 4: Parameters of the alternative electron transport materials

Parameter	Mg-TiO_2	Nb-TiO_2	Tm-TiO_2	Sn-TiO_2
Bandgap, Eg (eV)	3.22	3.18	2.6	3.0
Electron affinity, χ (eV)	4.2	4.15	3.9	3.9
Relative permittivity, εr	13.6	10	9	9
Electron mobility, μe ($cm^2\ V^{-1}\ s^{-1}$)	20	15	20	20
Hole mobility, μh ($cm^2\ V^{-1}\ s^{-1}$)	10	10	10	10
Donor density, ND (cm^{-3})	9.0×10^{20}	1.0×10^{18}	1.0×10^{16}	1.0×10^{19}
Defect density, Nt (cm^{-3})	1.0×10^{15}	1.0×10^{15}	1.0×10^{15}	1.0×10^{15}

Table 5: Parameters of the Alternative Whole Transport Materials

Parameter	CuI	Cu_2O	PEDOT:PSS	PTAA
Bandgap, Eg (eV)	3.1	2.17	1.6	2.96
Electron affinity, χ (eV)	2.1	3.2	3.4	2.3
Relative permittivity, εr	6.5	7.11	3	9
Electron mobility, μe ($cm^2\ V^{-1}\ s^{-1}$)	100	80	4.5×10^{-2}	1
Hole mobility, μh ($cm^2\ V^{-1}\ s^{-1}$)	43.9	80	4.5×10^{-2}	40
Acceptor density, NA (cm^{-3})	1.0×10^{18}	1.0×10^{18}	1.0×10^{18}	1.0×10^{18}
Donor density, ND (cm^{-3})	0	0	0	0
Defect density, Nt (cm^{-3})	1.0×10^{15}	1.0×10^{15}	1.0×10^{15}	1.0×10^{15}

Table 6: Recombination Coefficients Used For the Explicit Radiative and Auger Loss Simulations

Parameter	C343	TiO_2
Radiative recombination coefficient, Br	3.125×10^{-10} cm^3 s^{-1}	2.00×10^{-8} cm^3 s^{-1}
Electron Auger coefficient	1.221×10^{-28} cm^6 s^{-1}	2.00×10^{-24} cm^6 s^{-1}
Hole Auger coefficient	1.221×10^{-28} cm^6 s^{-1}	2.00×10^{-24} cm^6 s^{-1}

The optimization used a one at a time sweep, in which one parameter was varied while the remaining parameters were held at their baseline values. This approach was then followed by a consolidated optimized device calculation. The purpose was to separate changes caused by optical harvesting from those caused by transport and recombination. For the present loss study, the resulting architecture was FTO/Tm-TiO_2/C343/PEDOT: PSS/Au with 0.5 µm Tm-TiO_2, 0.7 µm C343, 0.5 µm PEDOT:PSS, and C343 bulk defect density of 1×10^{15} cm^{-3}. The subsequent non ideal simulations introduced temperature, Rs, Rsh, front reflection, and explicit radiative/Auger recombination sequentially before combining them.

RESULTS AND DISCUSSION

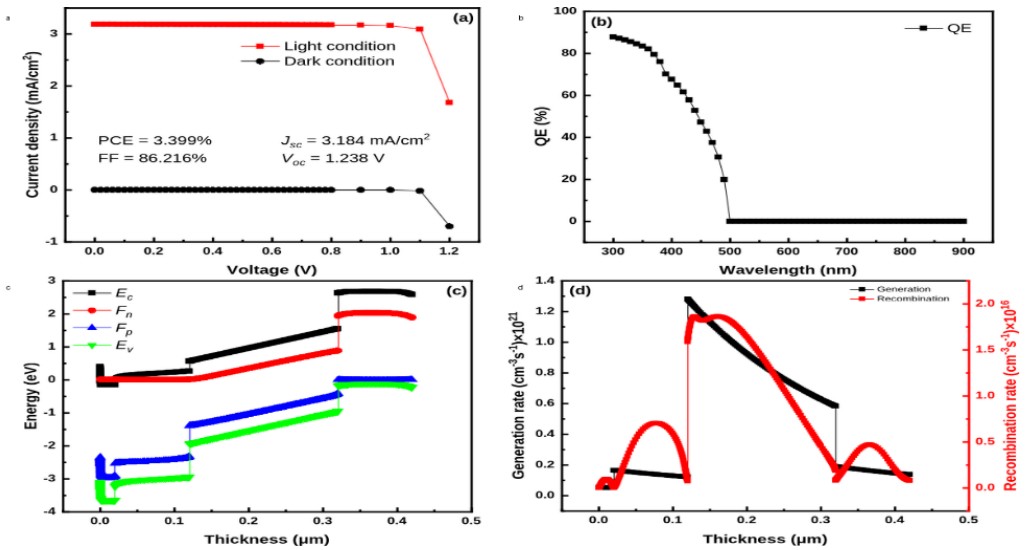


Figure 2: Reference C343 ssDSSC: (a) illuminated and dark J–V characteristics, (b) EQE spectrum, (c) energy band diagram, and (d) generation/recombination profiles

The reference FTO/TiO_2/C343/Spiro-OMeTAD/Au cell produced PCE at 3.399%, Jsc at 3.184 mA cm^{-2}, Voc at 1.238 V, and FF at 86.216% at 300 K and 100 mW cm^{-2}. These values are shown directly in Figure 2 and provide the starting point for the optimization. The relatively high FF indicates that the reference simulation contains limited ohmic distortion under the initial assumptions, whereas the much smaller Jsc points to incomplete photon harvesting and charge collection as the more immediate limitation. The EQE response is concentrated in the visible region, while the response falls at longer wavelengths because C343 and the wide bandgap TiO_2 do not efficiently use the lower energy part of the incident spectrum. More importantly for the present study, the generation and recombination curves in Figure 2d show that recombination is concentrated near the TiO_2/C343 interface.

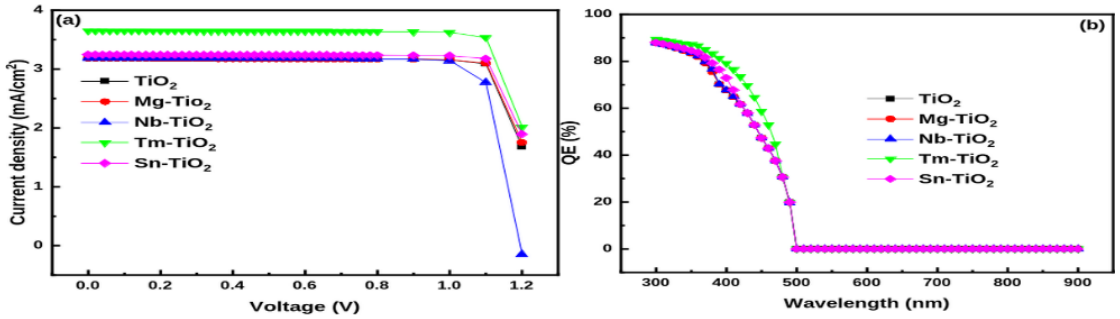


Figure 3. Comparison of pristine and doped TiO_2 electron transport layers: (a) J–V characteristics and (b) EQE spectra

Figure 3 shows that Tm-TiO_2 gave the strongest response among the investigated ETLs. Its peak EQE reached 89.3% at 300 nm, while the other doped variants followed at lower levels. The research attributes this improvement to the modification of the TiO_2 electronic structure by Tm incorporation and to associated changes in charge injection and trap related recombination (Tsotetsi et al., 2025). For a loss mechanism study, this selection matters because an ETL with weak extraction would make it difficult to distinguish intrinsic resistive losses from poor charge injection. The use of Tm-TiO_2 therefore establishes a relatively efficient electron pathway before temperature and parasitic resistance are deliberately introduced.

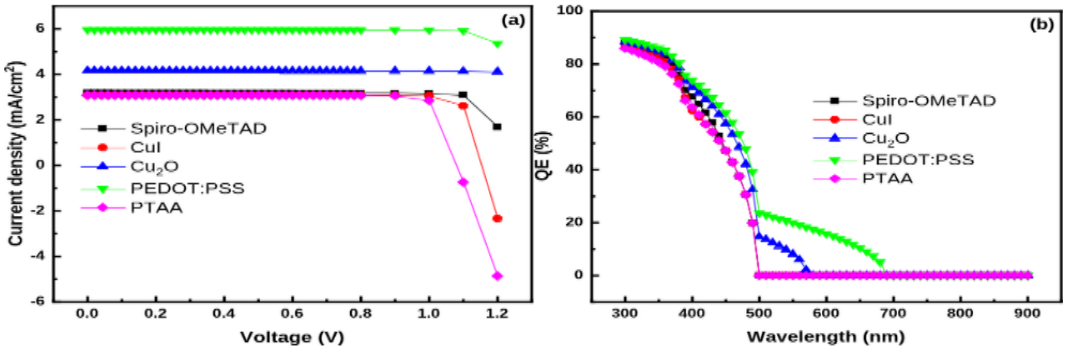


Figure 4. Comparison of solid state whole transport materials: (a) J–V characteristics and (b) EQE spectra

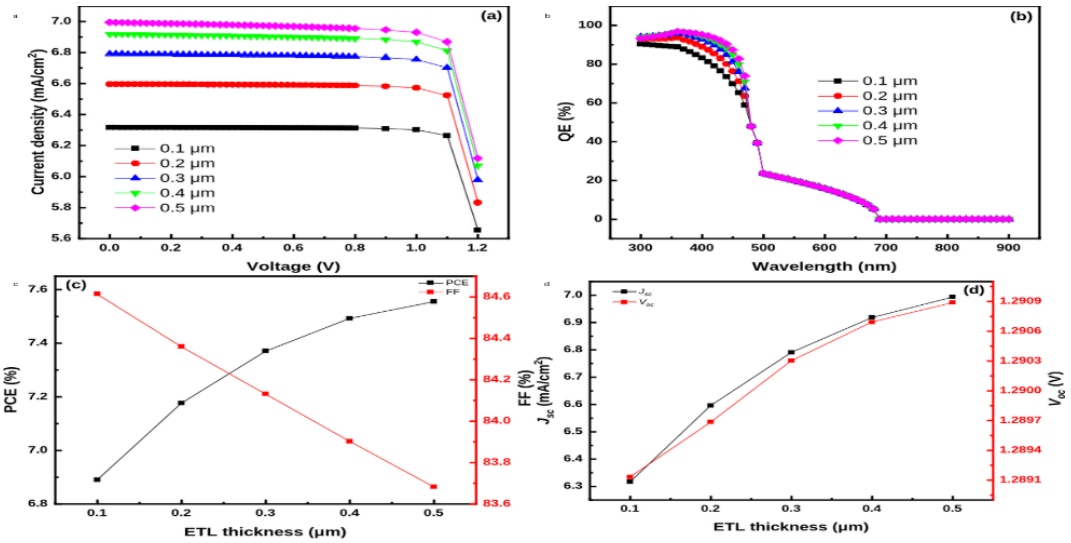


Figure 5. Effect of Tm-TiO_2 thickness on the optimized device: (a) J–V, (b) EQE, (c) PCE/FF, and (d) Jsc/Voc

Figure 5 shows that increasing the Tm-TiO_2 thickness from 0.1 to 0.5 µm increased Jsc from 6.32 to 6.99 mA cm^{-2} and raised Voc slightly from 1.2891 to 1.2900 V. The PCE increase was accompanied by an almost constant FF, indicating that the thicker ETL did not introduce a large ohmic penalty within the tested range. The near overlap of the 0.4 and 0.5 µm EQE curves also indicates that the optical benefit begins to saturate. Consequently, 0.5 µm was retained as the ETL thickness for the optimized device. This result is important for the series resistance analysis because it establishes that the selected ETL thickness was not itself producing a strong resistance driven loss in the optimization.

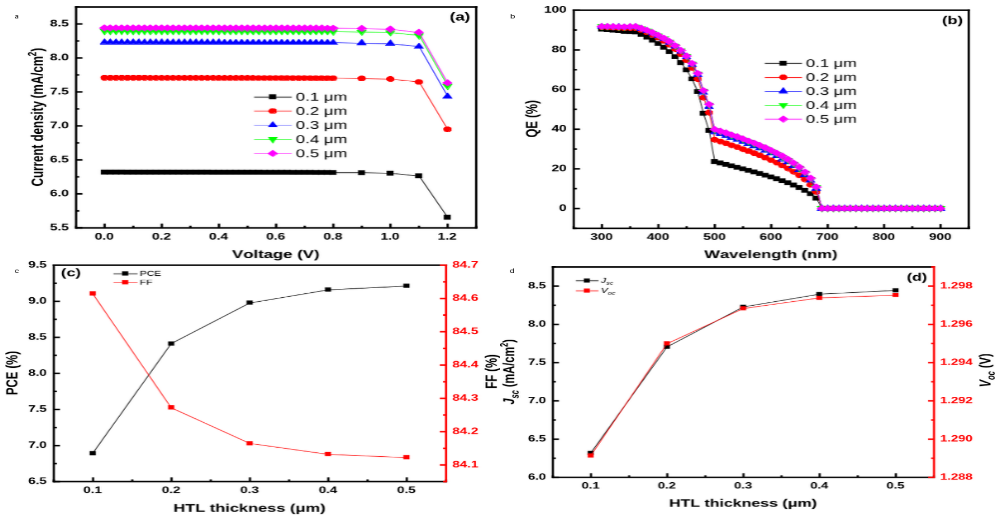


Figure 6. Effect of PEDOT:PSS thickness: (a) J–V, (b) EQE, (c) PCE/FF, and (d) Jsc/Voc

The PEDOT: PSS thickness sweep in Figure 6 produced a stronger electrical response as the layer increased from 0.1 to 0.5 µm. PCE rose from 6.89% to 9.21%, while Jsc increased from 6.32 to 8.44 mA cm^{-2} and Voc from 1.289 to 1.298 V. At the same time, FF declined slightly from 84.64% to 84.13%. The simultaneous improvement in current and voltage and the small reduction in FF indicate a competition between better interface coverage and increasing transport resistance. The 0.5 µm layer was selected because it gave the highest PCE in the tested range. The result also provides an early indication that resistive losses in the hole conducting layer should be evaluated separately after optimization.

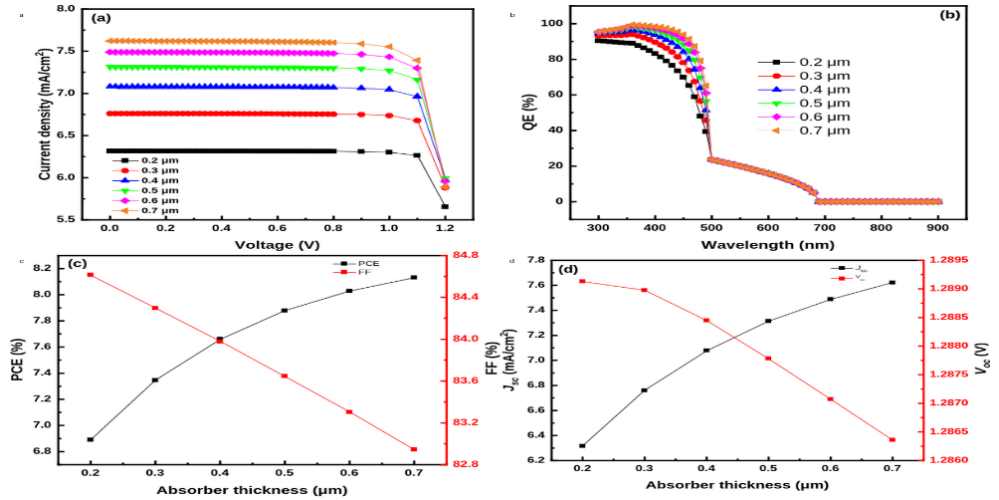


Figure 7. Effect of C343 absorber thickness: (a) J–V, (b) EQE, (c) PCE/FF, and (d) Jsc/Voc

As shown in Figure 7, increasing C343 thickness from 0.2 to 0.7 µm increased Jsc from 6.32 to 7.62 mA cm^{-2} and PCE from 6.89% to 8.13%. The EQE at 0.7 µm reached 99.3% at 360 nm. However, FF fell from 84.62% to 82.95%, and Voc decreased slightly from 1.289 to 1.286 V. The result illustrates a central feature of the device, more absorber material that improves photon capture, but increasing thickness also increases the opportunity for recombination and transport related losses. The 0.7 µm absorber was therefore adopted as the best value within the tested interval, rather than being treated as an absolute thickness optimum.

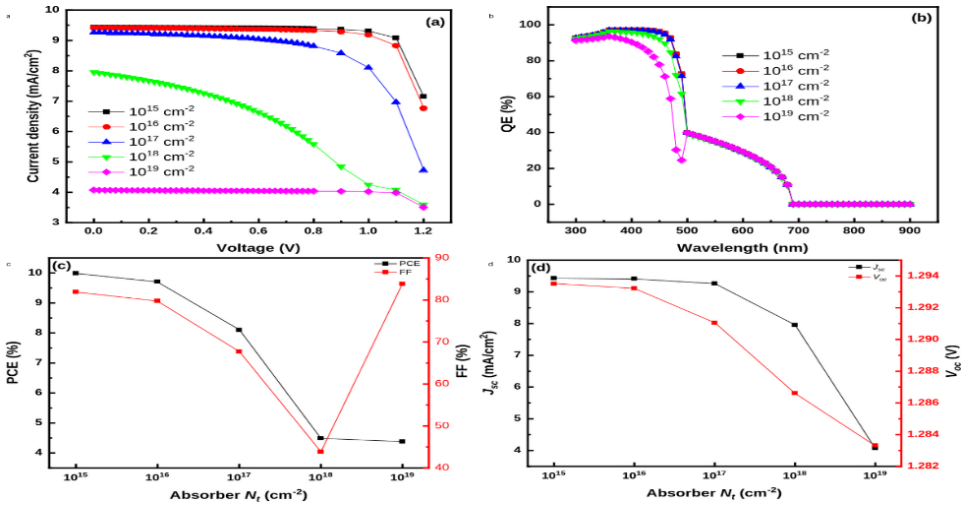


Figure 8. Effect of C343 bulk defect density: (a) J–V, (b) EQE, (c) PCE/FF, and (d) Jsc/Voc

The defect density sweep in Figure 8 gives a clearer indication of the recombination threshold. PCE remained about 9.99% at $N_t \leq 10^{15}$ cm^{-3} but declined to 4.38% at 10^{19} cm^{-3}. The most pronounced FF deterioration occurred between 10^{17} and 10^{18} cm^{-3}, where FF fell from 67.73% to 43.85%. Jsc remained close to 9.26 mA cm^{-2} up to 10^{17} cm^{-3} but declined to 4.07 mA cm^{-2} at 10^{19} cm^{-3}. Voc changed less dramatically, from about 1.293 to 1.283 V. This contrast between Jsc/FF and Voc is consistent with a defect controlled reduction in carrier lifetime and diffusion length, which first affects collection and maximum power operation before producing a comparably large voltage change (Hodes & Kamat, 2015; Jena & Bhargava, 2013). Maintaining N_t at or below 10^{15} cm^{-3} was used in the optimized device.

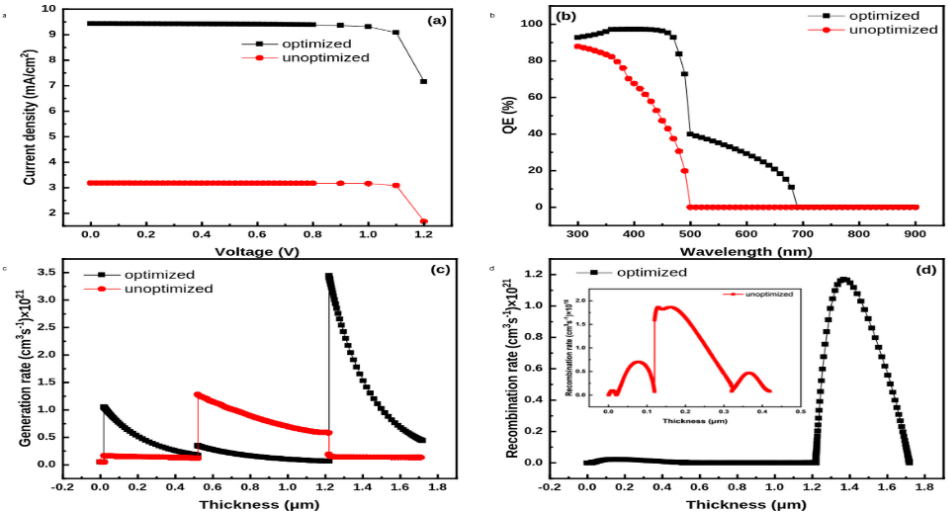


Figure 9. Optimized versus unoptimized device: (a) J–V, (b) EQE, (c) optical generation rate, and (d) recombination rate (source Figure 4.8).

Table 7. Comparison of the Unoptimized and Optimized C343 ssDSSC

Configuration	Voc (V)	Jsc (mA cm^{-2})	FF (%)	PCE (%)
Unoptimized reference	1.238	3.184	86.22	3.40
Optimized	1.294	9.430	81.90	9.99

The broader EQE tail observed in the optimized device should not be interpreted as a reduction in the intrinsic bandgap of C343. The HTL-screening results show that the extension toward longer wavelengths becomes pronounced after the introduction of PEDOT: PSS. In the SCAPS parameterization, PEDOT: PSS has a lower bandgap ($E_g = 1.6$ eV) than C343 ($E_g = 2.5$ eV), so the calculated spectral response reflects the complete

multilayer device rather than the C343 absorber alone. The long-wavelength tail is therefore attributed to the simulated response of the transport-layer environment, including possible photogeneration within PEDOT: PSS, rather than to a red-shift of the intrinsic C343 absorption edge.

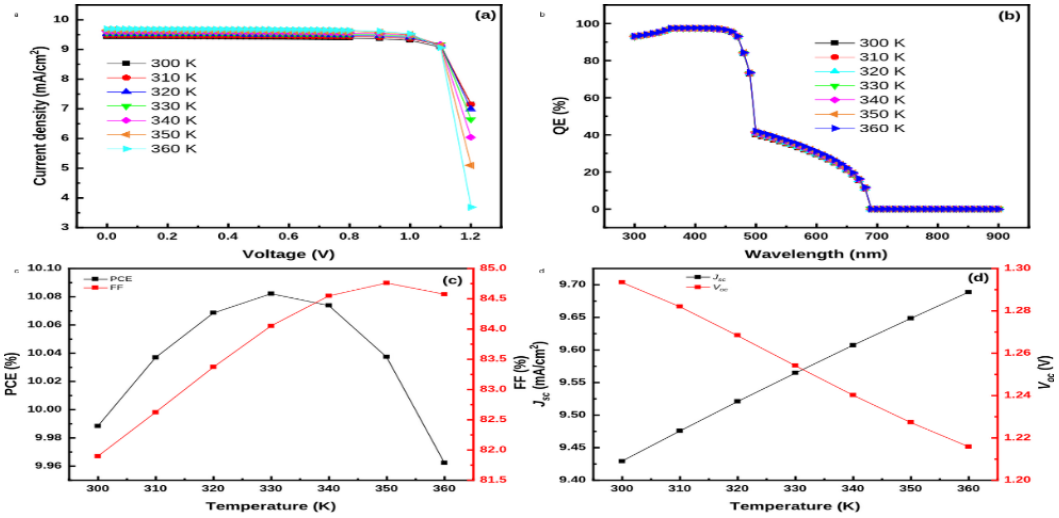


Figure 10. Temperature dependence of the optimized device: (a) J–V curves from 300–360 K, (b) EQE, (c) PCE/FF, and (d) Jsc/Voc (source Figure 4.9).

The thermal response in Figure 10 reveals a trade-off that is easy to miss when only the room temperature efficiency is considered. Between 300 and 360 K, Jsc increased from 9.43 to 9.69 mA cm^{-2}, corresponding to a positive coefficient of approximately 0.046% K^{-1}. The EQE spectra changed little across the temperature interval, with peak values near 97.2% at 400 nm. This means that the principal thermal penalty does not arise from a collapse of the spectral response. Instead, it appears mainly through voltage loss.

Voc decreased almost linearly from 1.294 V at 300 K to 1.216 V at 360 K, giving a temperature coefficient of approximately 1.3 mV K^{-1}. As temperature increases, the simulated device experiences greater carrier excitation and recombination, which increases the effective reverse saturation current and reduces the quasi-Fermi level splitting at open circuit (Green, 1982; Maçaira et al., 2015). At the same time, the PCE did not decrease immediately. Figure 10c shows an increase to about 10.08% at 330 K, followed by deterioration at higher temperature. The FF continues to improve toward the higher part of the range, which is associated with improved conductivity of PEDOT:PSS and electron transport in Tm-TiO_2. The combined result is therefore not a simple monotonic thermal response; modest transport gains initially compensate for the voltage penalty, but beyond about 330 K the voltage loss becomes dominant.

This temperature behavior is particularly relevant to deployment because a cell operating under strong sunlight can experience a temperature substantially above the nominal 300 K simulation point. The present results indicate that thermal management should be considered a performance variable rather than only a stability measure.

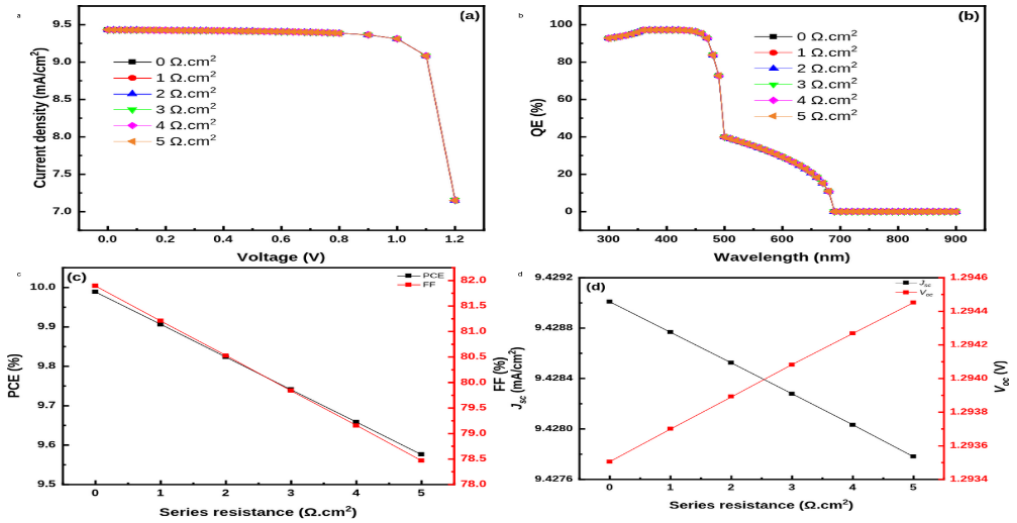


Figure 11: Series-resistance sensitivity: (a) J–V curves for Rs = 0–5 Ω cm², (b) EQE, (c) PCE/FF, and (d) Jsc/Voc

Figure 11 provides a clean separation between current generation and electrical dissipation. When Rs was increased from 0 to 5 Ω cm², the PCE decreased from 9.99% to 9.58%. The decline was approximately linear over the tested range and was driven mainly by FF. The Jsc changed only from 9.429 to 9.428 mA cm^{-2}, while Voc changed only within the numerical precision of the calculation. At the same time, the EQE curves remained almost identical and retained a peak near 97% at 400 nm. These three observations such as stable EQE, stable Jsc, and a declining FF identify Rs as an electrical rather than optical loss channel.

The practical significance of the result is that a device may retain an excellent spectral response while delivering less power because of internal voltage drops. This research identifies 2.0 Ω cm² as a useful critical resistance benchmark for experimental device development. Below this level, the change in PCE is comparatively modest; as resistance increases further, the fill-factor loss becomes more pronounced. This behavior agrees with the established dependence of fill factor on series resistance (Dadu et al., 2002; Green, 1982). Consequently, the selected 0.5 µm PEDOT:PSS layer should not be regarded simply as an optical or interfacial optimization. Its thickness also determines the electrical path through which holes reach the back contact.

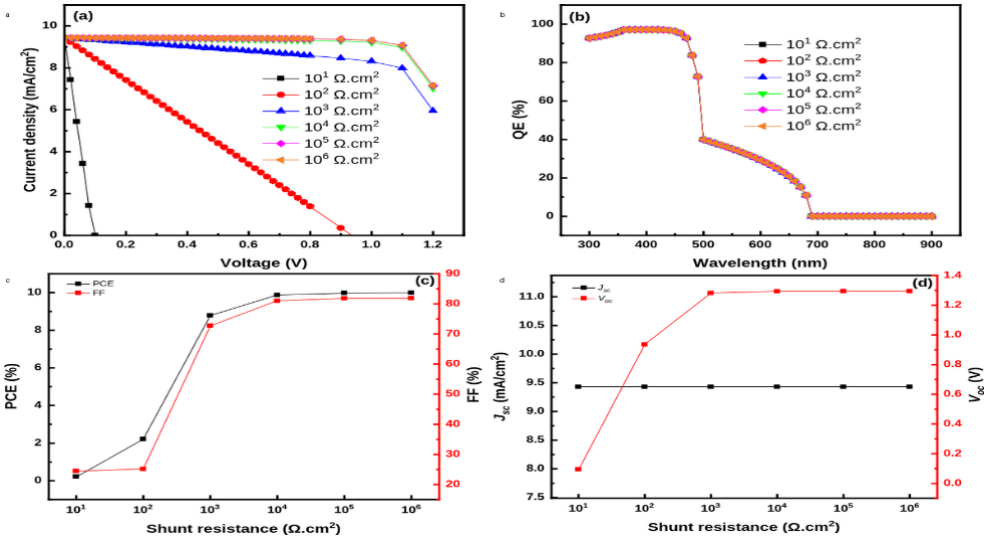


Figure 12: Shunt-resistance sensitivity: (a) J–V curves for Rsh = 10^1–10^6 Ω cm², (b) EQE, (c) PCE/FF, and (d) Jsc/Voc

The effect of Rsh in Figure 12 is much stronger than the effect of Rs over the ranges tested. At Rsh of 10^1 Ω cm², PCE was only 0.22%, but it increased to 9.99% at 10^6 Ω cm². Voc increased from 0.094 V at 10^1 Ω cm² to approximately 1.292 V at Rsh ≥ 10^3 Ω cm², whereas Jsc remained close to 9.429 mA cm⁻². The EQE curves were also nearly unchanged, with peak values around 97% between 360 and 400 nm. The separation between the stable EQE/Jsc and the rapidly changing Voc/FF shows that shunt leakage acts principally under finite bias and near open-circuit operation rather than by changing the amount of light absorbed.

At low Rsh, the leakage current bypasses the intended junction, so the quasi-Fermi level splitting cannot build to the value expected from the intrinsic material alignment. This explains why a device can have a favorable band structure and still produce a very low Voc. The rapid recovery of voltage once Rsh exceeds about 10^3 Ω cm² also suggests that suppressing physical shunts at interfaces and contacts should be a priority during fabrication. In contrast with Rs, which mainly reduces FF, low Rsh simultaneously attacks Voc and FF and can therefore produce a much larger PCE loss (Bisquert, 2002; Qin et al., 2024).

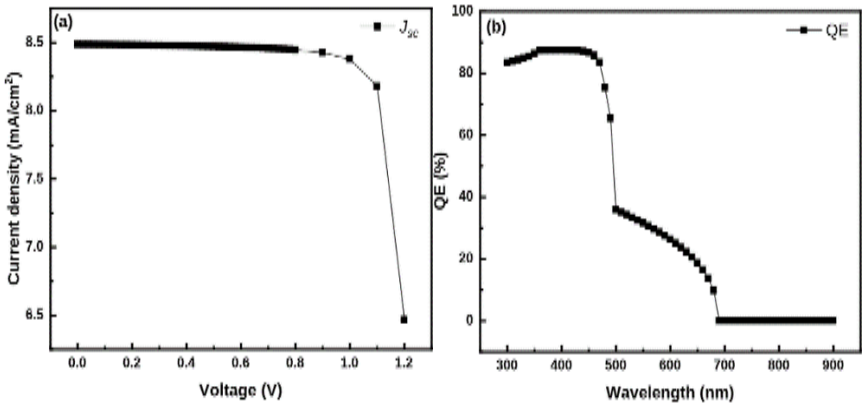


Figure 13. Effect of a 10% front optical reflection loss: (a) J–V characteristic and (b) EQE spectrum

Although reflection is not an electrical resistance, its effect is useful for separating photon-loss mechanisms from transport losses. With a 10% wavelength-independent reflection applied at the FTO front surface, Figure 13 shows that Voc was 1.291 V while Jsc fell from the ideal cumulative-loss baseline value of 9.565 to 8.486 mA cm⁻². The peak EQE was reduced from about 97% to 87% around 400 nm. The proportional decrease in current and EQE is consistent with a reduction in the number of photons entering the device rather than a change in the intrinsic charge-transfer energetics. Within the cumulative-loss sequence, the corresponding PCE decreased from the ideal baseline value of 10.081% to 8.996%, as shown in Table 8.

Because front reflection reduces the incident photon flux before it reaches the C343 layer, the generation rate throughout the principal photoactive region is reduced. Thus, an anti-reflective treatment can improve current without altering the absorber or transport-layer band structure. This is different from the Rs and Rsh cases, where the incident photon population and EQE can remain almost unchanged.

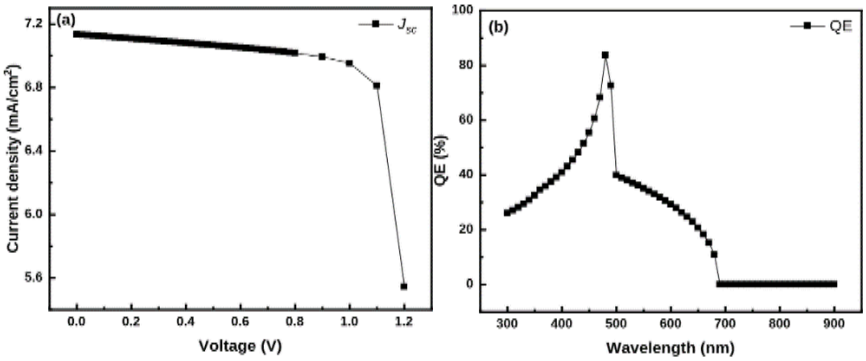


Figure 14: Explicit radiative and Auger recombination losses: (a) J–V characteristic and (b) EQE spectrum

Figure 14 isolates the effect of explicitly activating radiative and Auger recombination. Voc decreases slightly from 1.294 to 1.289 V, a change of 5 mV, but Jsc decreases much more strongly from 9.430 to 7.134 mA cm^{-2}, a reduction of 24.35%. The PCE falls to 7.492%, while FF remains close to 81.5% as shown in Table 8. This contrast shows that recombination is principally removing photogenerated carriers before collection rather than producing a large additional resistive distortion of the J–V curve.

The EQE response in Figure 14b is not uniformly scaled in the same way as the reflection case. The suppression becomes somewhat stronger toward longer wavelengths. Within the simulated structure, longer wavelength photons generate carriers deeper in the active layer, increasing the distance over which carriers must travel before reaching selective contacts and therefore increasing the opportunity for recombination. The result is consistent with the carrier density dependence of radiative and Auger processes and with the broader role of recombination in limiting charge collection (Bisquert, 2002; Yang et al., 2024). Taken together with the defect density sweep in Figure 8, the result confirms that recombination operates on more than one scale, showing bulk defects shorten carrier lifetime, while explicit radiative/Auger channels provide additional loss routes when carrier populations are sufficiently high.

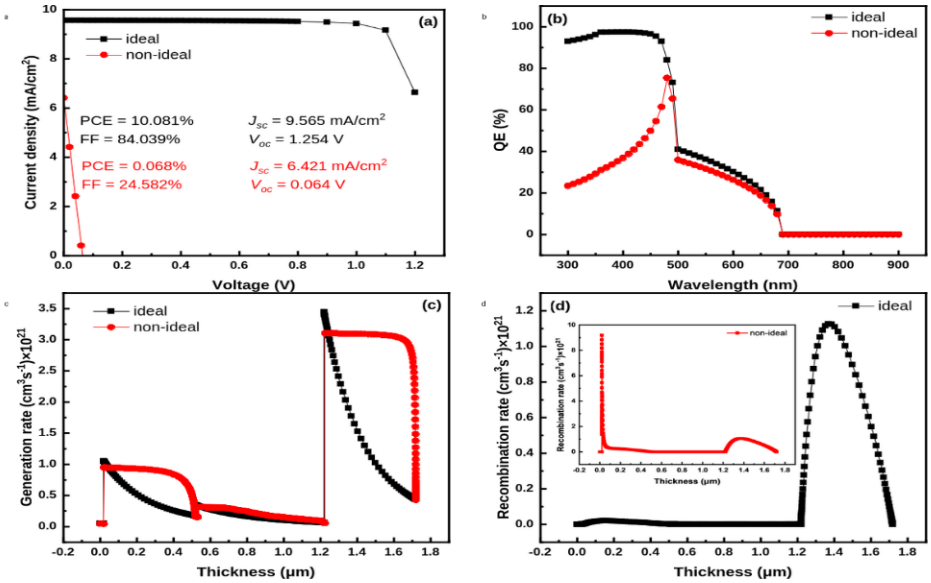


Figure 15. Ideal versus fully non-ideal device: (a) J–V, (b) EQE, (c) generation rate, and (d) recombination rate

Table 8: Simulated Ideal and Non-Ideal Performance States

Simulation condition	Voc (V)	Jsc (mA cm^{-2})	FF (%)	PCE (%)
Idealized loss-analysis baseline	1.254	9.565	84.039	10.081
10% reflection	1.291	8.486	82.092	8.996
Radiative + Auger recombination	1.289	7.134	81.485	7.492
Series + shunt resistance	0.094	6.285	24.795	0.147
Fully non-ideal condition	0.064	6.421	24.582	0.068

The cumulative comparison in Figure 15 and Table 8 is the clearest indication of which losses dominate the modeled device. The ideal configuration gives 10.081% PCE with Jsc = 9.565 mA cm^{-2}, Voc = 1.254 V, and FF = 84.039%. Adding 10% reflection reduces PCE to 8.996%, mainly through the loss of current. Adding radiative and Auger recombination reduces PCE further to 7.492%, with a pronounced reduction in Jsc. By contrast, introducing the modeled resistance terms reduces PCE to only 0.147%, with Voc falling to 0.094 V and FF to 24.795%. The fully non-ideal case then reaches only 0.068% PCE, with Voc = 0.064 V and FF = 24.582%.

The scale of the resistance penalty is striking because the earlier individual sweeps showed that moderate Rs alone produces only a small PCE change, whereas very low Rsh causes catastrophic degradation. The combined resistance case therefore reflects the dominance of shunt leakage in the severe non-ideal regime. The drop in Jsc from 9.565 to 6.421 mA cm^{-2} in the fully non-ideal device also shows that once leakage and recombination are present together,

current collection is no longer protected by the favorable ideal optical response.

The EQE comparison in Figure 15b reinforces this conclusion. The ideal device reaches a peak EQE of 97.4% at 400 nm, whereas the non-ideal device has a peak of about 75.3% near 480 nm. The suppression across the absorption range indicates that the loss mechanisms are not confined to a narrow spectral interval. Figure 15c further shows the reduction of the optical generation profile in the active region when reflection is present, while Figure 15d shows the emergence of strong recombination features near the front interface and within the bulk. The resulting picture is therefore a coupled one: optical loss reduces carrier generation, defects and explicit recombination reduce carrier survival, and parasitic resistance prevents the surviving carriers from being converted efficiently into useful electrical power.

CONCLUSION

This numerical study examined the thermal and resistive limits of a Coumarin-343-based solid-state dye-sensitized solar cell by building the loss analysis around an optimized FTO/Tm-TiO_2/C343/PEDOT:PSS/Au structure. The reference device produced 3.399% PCE, while systematic material and geometrical optimization raised the simulated efficiency to 9.99%, with Voc = 1.294 V, Jsc = 9.430 mA cm^{-2}, and FF = 81.90%. The improvement was obtained by selecting Tm-TiO_2 and PEDOT: PSS, using 0.5 µm and 0.5 µm transport-layer thicknesses, respectively, a 0.7 µm C343 layer, and a C343 defect density of 1×10^{15} cm^{-3}.

The loss analysis shows that temperature, series resistance, shunt resistance, optical reflection, and recombination do not affect the device in the same way. Between 300 and 360 K, Jsc increased slightly but Voc fell by 78 mV, giving a temperature coefficient of −1.3 mV K^{-1}; the highest simulated PCE occurred around 330 K. Series resistance from 0 to 5 Ω cm^2 reduced PCE only from 9.99% to 9.58% and acted mainly through FF. Shunt resistance was far more consequential when PCE increased from 0.22% at 10^1 Ω cm^2 to 9.99% at 10^6 Ω cm^2, while Voc rose from 0.094 to about 1.292 V. Ten-percent front reflection reduced Jsc by 10%, whereas explicit radiative and Auger recombination reduced Jsc by 24.35% and PCE to 7.492%.

The most important result is the cumulative loss response. The ideal cumulative-loss baseline reached 10.081% PCE, but the fully non-ideal configuration fell to 0.068%. The severe degradation was dominated by parasitic resistance, particularly low shunt resistance, and was reinforced by recombination and optical losses. However, the study remains a numerical SCAPS-1D analysis and has not yet been experimentally validated for fabricated C343-based ssDSSCs. In addition, the combined loss case was used to show the cumulative impact of selected non-ideal inputs, but it does not fully resolve possible non-additive or synergistic interactions among loss mechanisms, such as temperature-dependent recombination coefficients or field-dependent leakage pathways in a real device. For future experimental work, the numerical results therefore point to four priorities: suppressing interfacial shunts, keeping series resistance low, maintaining C343 and interface defect densities near the optimized values, and controlling operating temperature and front-surface reflection. These measures are more important than simply increasing layer thickness once the main optical and transport gains have already been obtained.

REFERENCES

Arya, S., & Mahajan, P. (2023). Introduction to solar cells. In S. Arya & P. Mahajan, Solar cells (pp. 1–35). Springer Nature Singapore. https://doi.org/10.1007/978-981-99-7333-0_1

Benesperi, I., Michaels, H., & Freitag, M. (2018). The researcher's guide to solid-state dye-sensitized solar cells. Journal of Materials Chemistry C, 6(44), 11903–11942. https://doi.org/10.1039/C8TC03542C

Bisquert, J. (2002). Theory of the impedance of electron diffusion and recombination in a thin layer. The Journal of Physical Chemistry B, 106(2), 325–333. https://doi.org/10.1021/jp011941g

Boschloo, G. (2019). Improving the performance of dye-sensitized solar cells. Frontiers in Chemistry, 7, 77. https://doi.org/10.3389/fchem.2019.00077

Burgelman, M., Nollet, P., & Degrave, S. (2000). Modelling polycrystalline semiconductor solar cells. Thin Solid Films, 361–362, 527–532. https://doi.org/10.1016/S0040-6090(99)00825-1

Dadu, M., Kapoor, A., & Tripathi, K. N. (2002). Effect of operating current dependent series resistance on the fill factor of a solar cell. Solar Energy Materials and Solar Cells, 71(2), 213–218. https://doi.org/10.1016/S0927-0248(01)00059-9

Danladi, E., Kashif, M., Daniel, T., Achem, C., Alpha, M., & Gyan, M. (2022). 7.379% power conversion efficiency of a numerically simulated solid-state dye-sensitized solar cell with copper (I) thiocyanate as a whole conductor. East European Journal of Physics, (3), 19–31. https://doi.org/10.26565/2312-4334-2022-3-03

Danladi, E., Obagboye, L. F., Aisida, S., Ezema, F. I., Okorie, O., Bwamba, J. A., Emmanuel, P. A., Hussaini, A. A., Jubu, P. R., & Ozurumba, A. C. (2024). 20.730% highly efficient lead-free CsSnI3-based perovskite solar cells with various charge transport materials: A SCAPS-

1D study. Multiscale and Multidisciplinary Modeling, Experiments and Design, 8(1), 114. https://doi.org/10.1007/s41939-024-00701-2

Dehghani, N., Jamekhorshid, A., Jalali, T., & Osfouri, S. (2025). Numerical modeling of charge transfer and recombination kinetics in the dye-sensitized solar cell: Conceptual integration of optics, electricity, and electrochemistry. Renewable Energy, 239, 122150. https://doi.org/10.1016/j.renene.2024.122150

Green, M. A. (1982). Solar cells: Operating principles, technology, and system applications. https://www.osti.gov/biblio/6051511

Hagfeldt, A., Boschloo, G., Sun, L., Kloo, L., & Pettersson, H. (2010). Dye-sensitized solar cells. Chemical Reviews, 110(11), 6595–6663. https://doi.org/10.1021/cr900356p

Hodes, G., & Kamat, P. V. (2015). Understanding the implication of carrier diffusion length in photovoltaic cells. The Journal of Physical Chemistry Letters, 6(20), 4090–4092. https://doi.org/10.1021/acs.jpclett.5b02052

Hu, L., Song, J., Yin, X., Su, Z., & Li, Z. (2020). Research progress on polymer solar cells based on PEDOT:PSS electrodes. Polymers, 12(1), 145. https://doi.org/10.3390/polym12010145

Jena, A. K., & Bhargava, P. (2013). Effect of amount of dye in the TiO2 photoanode on electron transport, recombination, Jsc and Voc of dye-sensitized solar cells. RSC Advances, 3(8), 2655–2661. https://doi.org/10.1039/C2RA22465H

Johansson, E. M. J., Sandell, A., Siegbahn, H., Rensmo, H., Mahrov, B., Boschloo, G., Figgemeier, E., Hagfeldt, A., Jönsson, S. K. M., & Fahlman, M. (2005). Interfacial properties of photovoltaic TiO2/dye/PEDOT–PSS heterojunctions. Synthetic Metals, 149(2–3), 157–167. https://doi.org/10.1016/j.synthmet.2004.12.004

Karaca, Ç., Bardak, F., Köse, E., & Ataç, A. (2025). Experimental and computational insights into the electronic structures and absorption-emission characteristics of coumarin, C-6H, C-153, and C-343 dyes. Spectrochimica Acta Part A: Molecular and Biomolecular Spectroscopy, 335, 125995. https://doi.org/10.1016/j.saa.2025.125995

Kokkonen, M., Talebi, P., Zhou, J., Asgari, S., Soomro, S. A., Elsehrawy, F., Halme, J., Ahmad, S., Hagfeldt, A., & Hashmi, S. G. (2021). Advanced research trends in dye-sensitized solar cells. Journal of Materials Chemistry A, 9(17), 10527–10545. https://doi.org/10.1039/D1TA00690H

Koops, S. E., Barnes, P. R. F., O'Regan, B. C., & Durrant, J. R. (2010). Kinetic competition in a coumarin dye-sensitized solar cell: Injection and recombination limitations upon device performance. The Journal of Physical Chemistry C, 114(17), 8054–8061. https://doi.org/10.1021/jp910972x

Kumari Shukla, V., & Sekar, N. (2024). Effect of 3,4-ethylenedioxythiophene (EDOT) as bridged spacer on DSSC and nonlinear optical properties: A DFT approach. ChemistrySelect, 9(7), e202305088. https://doi.org/10.1002/slct.202305088

Liu, X., Cole, J. M., Waddell, P. G., Lin, T.-C., & McKechnie, S. (2013). Molecular origins of optoelectronic properties in coumarins 343, 314T, 445, and 522B. The Journal of Physical Chemistry C, 117(27), 14130–14141. https://doi.org/10.1021/jp400614e

Maçaira, J., Andrade, L., & Mendes, A. (2014). Modeling, simulation and design of dye sensitized solar cells. RSC Advances, 4(6), 2830–2844. https://doi.org/10.1039/C3RA46295A

Maçaira, J., Mesquita, I., Andrade, L., & Mendes, A. (2015). Role of temperature in the recombination reaction on dye-sensitized solar cells. Physical Chemistry Chemical Physics, 17(35), 22699–22710. https://doi.org/10.1039/C5CP02942B

Nam, S.-H., Ju, D.-W., & Boo, J.-H. (2024). Variations in power conversion efficiency on n-type dye-sensitized solar cells with synthesized TiO2 nanoparticle: A thickness effect of active layer. Catalysts, 14(9), 598. https://doi.org/10.3390/catal14090598

Nguyen, T. T., Tran, V. N., & Bach, T. C. (2014). Influences of metallic doping on anatase crystalline titanium dioxide: From electronic structure aspects to efficiency of TiO2-based dye sensitized solar cell (DSSC). Materials Chemistry and Physics, 144(1–2), 114–121. https://doi.org/10.1016/j.matchemphys.2013.12.025

O'Regan, B. C., & Durrant, J. R. (2009). Kinetic and energetic paradigms for dye-sensitized solar cells: Moving from the ideal to the real. Accounts of Chemical Research, 42(11), 1799–1808. https://doi.org/10.1021/ar900145z

Palomares, E., Clifford, J. N., Haque, S. A., Lutz, T., & Durrant, J. R. (2002). Slow charge recombination in dye-sensitised solar cells (DSSC) using Al2O3 coated

nanoporous TiO2 films. Chemical Communications, (14), 1464–1465. https://doi.org/10.1039/b202515a

Qin, D., Qiu, M., & Zhan, X. (2024). Determining shunt resistances via modeling the photovoltaic performance of organic solar cells. Journal of Materials Chemistry A, 12(25), 15063–15070. https://doi.org/10.1039/D3TA08029C

Saidarsan, A., Guruprasad, S., Malik, A., Basumatary, P., & Ghosh, D. S. (2025). A critical review of unrealistic results in SCAPS-1D simulations: Causes, practical solutions and roadmap ahead. Solar Energy Materials and Solar Cells, 279, 113230. https://doi.org/10.1016/j.solmat.2024.113230

Shahrim, N. A., Ahmad, Z., Wong Azman, A., Fachmi Buys, Y., & Sarifuddin, N. (2021). Mechanisms for doped PEDOT:PSS electrical conductivity improvement. Materials Advances, 2(22), 7118–7138. https://doi.org/10.1039/D1MA00290B

Shanmugam, N., Pugazhendhi, R., Madurai Elavarasan, R., Kasiviswanathan, P., & Das, N. (2020). Anti-reflective coating materials: A holistic review from PV perspective. Energies, 13(10), 2631. https://doi.org/10.3390/en13102631

Tsotetsi, D., Idisi, D. O., Rono, N., Meyer, E. L., Benecha, E. M., Mbule, P., & Dhlamini, M. (2025). An experimental and computational investigation of thulium doped TiO2 as n-type material for potential application in bulk heterojunction organic solar cells. Materials for Renewable and Sustainable Energy, 14(1), 28. https://doi.org/10.1007/s40243-025-00304-y

Wang, J., Li, M., Qi, D., Shen, W., He, R., & Lin, S. H. (2014). Exploring photophysical properties of metal-free coumarin sensitizers: An efficient strategy to improve the performance of dye-sensitized solar cells. RSC Advances, 4(96), 53927–53938. https://doi.org/10.1039/C4RA07904C

Wang, N., Hu, J., Gao, L., & Ma, T. (2020). Current progress in solid-state electrolytes for dye-sensitized solar cells: A mini-review. Journal of Electronic Materials, 49(12), 7085–7097. https://doi.org/10.1007/s11664-020-08483-2

Yang, Q., Bittkau, K., Eberst, A., Rau, U., & Ding, K. (2024). The impact of interface recombination on the external quantum efficiency of silicon solar cells. Solar Energy Materials and Solar Cells, 273, 112953. https://doi.org/10.1016/j.solmat.2024.112953

Zaine, S. N. A., Mohamed, N. M., Khatani, M., Samsudin, A. E., & Shahid, M. U. (2020). Trap state and charge recombination in nanocrystalline passivized conductive and photoelectrode interface of dye-sensitized solar cell. Coatings, 10(3), 284. https://doi.org/10.3390/coatings10030284

Zhang, C.-R., Liu, L., Liu, Z.-J., Shen, Y.-L., Sun, Y.-T., Wu, Y.-Z., Chen, Y.-H., Yuan, L.-H., Wang, W., & Chen, H.-S. (2012). Electronic structures and optical properties of organic dye sensitizer NKX derivatives for solar cells: A theoretical approach. Journal of Molecular Graphics and Modelling, 38, 419–429. https://doi.org/10.1016/j.jmgm.2012.09.004